Atomistic Study of a CaTiO3-Based Mixed Conductor: Defects, Nanoscale Clusters, and Oxide-Ion Migration

ARTICLE *in* ADVANCED FUNCTIONAL MATERIALS · JANUARY 2007

Impact Factor: 11.81 · DOI: 10.1002/adfm.200600632

3 AUTHORS:

G. C. Mather
Institute of Ceramics and Glass
86 PUBLICATIONS **1,080** CITATIONS

SEE PROFILE

M. Saiful Islam
University of Bath
173 PUBLICATIONS **7,378** CITATIONS

SEE PROFILE

F. M. Figueiredo
University of Aveiro
133 PUBLICATIONS **1,991** CITATIONS

SEE PROFILE

ADVANCED FUNCTIONAL MATERIALS

DOI: 10.1002/adfm.200600632

Atomistic Study of a $CaTiO_3$-Based Mixed Conductor: Defects, Nanoscale Clusters, and Oxide-Ion Migration**

By *Glenn C. Mather*,* *M. Saiful Islam*, and *Filipe M. Figueiredo*

Mixed oxide-ion and electronic conductivity can be exploited in dense ceramic membranes for controlled oxygen separation as a means of producing pure oxygen or integrating with catalytic oxidation. Atomistic simulation has been used to probe the energetics of defects, dopant-vacancy association, nanoscale cluster formation, and oxide-ion transport in mixed-conducting $CaTiO_3$. The most favorable energetics for trivalent dopant substitution on the Ti site are found for Mn^{3+} and Sc^{3+}. Dopant-vacancy association is predicted for pair clusters and neutral trimers. Low binding energies are found for Sc^{3+} in accordance with the high oxide-ion conductivity of Sc-doped $CaTiO_3$. The preferred location for Fe^{4+} is in a hexacoordinated site, which supports experimental evidence that Fe^{4+} promotes the termination of defect chains and increases disorder. A higher oxide-ion migration energy for a vacancy mechanism is predicted along a pathway adjacent to an Fe^{3+} ion rather than Fe^{4+} and Ti^{4+}, consistent with the higher observed activation energies for ionic transport in reduced $CaTi(Fe)O_{3-\delta}$.

1. Introduction

Calcium titanate is well known for giving its mineral name, perovskite, to the vast family of isostructural compounds (ABO_3) with key properties for materials applications. In many research fields, $CaTiO_3$ itself is an important material.[1–3] For example, upon acceptor doping with a lower-valence cation, calcium titanate exhibits oxide-ion and electronic mixed conduction;[4–6] a relatively common occurrence in perovskite oxides with transition metal B-site cations. The undoped material is an incipient ferroelectric[7] with potential application in microwave-tunable devices,[8] but on doping with Pb it becomes a true ferroelectric.[9] The versatility of calcium titanate extends to its suitability as a material for the immobilization of radioactive waste[10] and a biocompatible coating for medical Ti implants.[11]

The mixed oxide-ion and electronic conductivity of $CaTiO_3$ can be exploited in dense ceramic membranes for controlled oxygen separation as a means of producing pure oxygen or for integrating with catalytic oxidation, as described in recent reviews.[12] An important potential application is the partial oxidation of methane to syngas (a mixture of CO and H_2). Iron-substituted calcium titanate ($CaTi(Fe)O_{3-\delta}$) is one of the most promising systems under development[13,14] because of its superior mechanical and chemical stability under a wide range of oxygen chemical potentials and low cost in comparison with competing systems, such as $La_{1-x}Sr_xCo_{1-y}Fe_yO_{3-\delta}$.[15,16]

Mixed conduction in $CaTi_{1-x}Fe_xO_{3-\delta}$ was first studied by Iwahara and co-workers,[4] who found a maximum ionic conductivity for $x \approx 0.20$ (ca. 0.1 S cm^{-1} at 1000 °C). Early interpretations of the electrical properties were based on noninteracting point defects where the substitution of Ti^{4+} with Fe^{3+} is compensated by the formation of oxygen vacancies and electrons (at low oxygen partial pressures, pO_2) or holes (at high pO_2). However, these models fail to explain the maximum in ionic conductivity at a relatively low Fe content.

Detailed structural studies by Grenier et al.,[17] published ten years before the first conductivity work, provide a more satisfactory interpretation based on extended vacancy-ordered defects. For Fe contents up to approximately 25 at %, the oxygen vacancies tend to remain disordered, or partially ordered, and thus participate in ionic transport. Significant ordering takes place for higher iron contents, which eventually leads to the formation of fully ordered phases when $x \geq 0.5$. These phases can be described by the general formula $A_nB_nO_{3n-1}$, and consist of a succession of BO_6 octahedra, primarily occupied by Ti^{4+}, and BO_4 tetrahedra, occupied by Fe^{3+}, ordered in layers perpendicular to the longest axis of the orthorhombic parent

[*] Dr. G. C. Mather
Instituto de Cerámica y Vidrio, CSIC
Cantoblanco, 28049 Madrid (Spain)
E-mail: mather@icv.csic.es
Prof. M. S. Islam
Department of Chemistry
University of Bath
Bath BA2 7 AY (UK)
Dr. F. M. Figueiredo
Departamento de Eng. Cerâmica e do Vidro, CICECO
Universidade de Aveiro
Aveiro 3810-193 (Portugal)
Dr. F. M. Figueiredo
Departamento de Ciências Exactas e Tecnológicas
Universidade Aberta
Lisbon 1269-001 (Portugal)

[**] We thank the ESF OSSEP programme (Optimization of Solid State Electrochemical Processes for Hydrocarbon Oxidation) for financial support, and Dr. Craig Fisher for useful discussions. Supporting Information is available online from Wiley InterScience or from the author.

structure. Oxide-ion conductivity is highest for iron contents lower than $x \approx 0.4$, where the low-temperature structure (< 1000 °C) is partially ordered in linear defect clusters of length less than 10 nm; these clusters are likely to consist of oxygen vacancies and tetrahedral Fe^{3+}.[5,18] The defect chains form along three perpendicular directions in a complex disordered microdomain texture that develops according to the temperature, the oxygen stoichiometry and, in turn, the Fe coordination and oxidation states. In addition to tetrahedral Fe^{3+} sites, the partially ordered phases exhibit penta- and hexacoordinated Fe^{3+},[19,20] and a variable fraction of Fe^{4+} that appears to have an important influence on the microstructure and consequently on the transport properties.[5,21]

A greater fundamental knowledge of defect clustering and vacancy migration on the atomic level in $CaTiO_3$-based systems is required to understand the rather complex structure–property relationships. Atomistic simulation techniques are well-suited to studying defect properties on this scale, as demonstrated in previous simulations of oxide-ion and proton conductors such as $LaGaO_3$[22,23] and $BaCeO_3$.[24,25] Herein, we have employed a wide-ranging sequence of atomistic simulations to address a number of important topics concerning pure and substituted $CaTiO_3$, with particular attention paid to its application as a mixed-conducting membrane. These include the energetic and mechanistic features of intrinsic defects, dopant incorporation, defect-cluster formation and oxide-ion migration.

2. Results and Discussion

2.1. Intrinsic Atomic Defects

Calculations were performed to determine the energies of isolated intrinsic defects (vacancies and interstitials) in $CaTiO_3$, from which Frenkel- and Schottky-type defect energies could be derived. The lattice energies used in the calculation of Schottky-type defects were taken from atomistic simulations of CaO, TiO_2[26] and $CaTiO_3$ (this work).

Examination of Table 1 reveals that the formation of oxygen vacancies in $CaTiO_3$ requires a similar amount of energy for both O1 and O2 sites. Schottky defects are highly unfavorable, supporting the hypothesis that the electrical conduction in undoped $CaTiO_3$ is greatly influenced by the presence of small amounts of acceptor impurities.[27–29] Although the lowest-energy defect type is the formation of a pair of Ca and O vacancies, the magnitude of the energy suggests such defects are present in negligible concentration; we may note that this V_A''–$V_O^{\bullet\bullet}$ defect is significantly more favorable in the related $SrTiO_3$[30] and $CaZrO_3$[31] systems. In addition, anion and cation Frenkel defects were investigated and found to be highly unfavorable (> 3.6 eV), as expected for the close-packed perovskite structure.

In the Fe-substituted phase, oxygen vacancies placed adjacent to the defect cluster are of lower energy than those isolated from the cluster (Table 1). The isolated vacancies have similar energy for both oxygen sites, whereas the O2 position is of lower energy for vacancies adjacent to the cluster. The preference of the vacancy for the O2 position accords with the formation of brownmillerite-type defects in the (0*k*0) planes of the orthorhombic parent phase (space group, *Pnma*) with increasing dopant and oxygen-vacancy concentration.[17]

Table 1. Calculated defect energies for $CaTiO_3$ and $CaTi_{0.8}Fe_{0.2}O_{3-\delta}$.

(a) point defects

Defect	Energy [eV] [a]		
	$CaTiO_3$	$CaTi_{0.8}Fe_{0.2}O_{3-\delta}$	
		isolated from cluster	adjacent to cluster
Ca vacancy	22.15	22.17	19.52
Ti vacancy	82.27	81.78	79.51
O1 vacancy	19.64	19.68	18.62
O2 vacancy	19.63	19.48	17.63

(b) Schottky disorder

Type	Defect equilibrium	Energy [eV/defect]	
		$CaTiO_3$	$CaTi_{0.8}Fe_{0.2}O_{3-\delta}$ [b]
Schottky	$Ca_{Ca}^{\times} + Ti_{Ti}^{\times} + 3O_O^{\times} = V_{Ca}'' + V_{Ti}'''' + 3V_O^{\bullet\bullet} + CaTiO_3$	2.49	2.30
Ca Schottky	$Ca_{Ca}^{\times} + O_O^{\times} = V_{Ca}'' + V_O^{\bullet\bullet} + CaO$	2.92	2.85
Ti Schottky	$Ti_{Ti}^{\times} + 2O_O^{\times} = V_{Ti}'''' + 2V_O^{\bullet\bullet} + TiO_2$	3.03	2.76

[a] Reference at infinity. [b] Schottky disorder isolated from cluster.

2.2. Dopant-Ion Substitution and Dopant-Vacancy Association

Significant oxide-ion conductivity is observed in calcium titanate on replacing Ti with a lower valence cation to form mobile oxygen vacancies. The relative energies of "solution" of a series of trivalent and divalent cations were evaluated by combining the appropriate defect and lattice-energy terms[26,32–34] and are shown in Table 2. The most favorable solution energies are found for Sc^{3+} and Mn^{3+}, with the largest energies being those of divalent species Fe^{2+} and Ni^{2+}.

It is well-known that the charge-compensating oxygen vacancies, which form on acceptor doping, tend to interact favorably with the dopant, leading to defect clustering. Formation of such clusters adds an additional binding (or association) term to the activation energy for oxide-ion conductivity. A previous study of fluorite-structured ZrO_2[35] has shown that the configuration of the defect cluster depends on the size of the dopant cation,

Table 2. Calculated incorporation (solution) energies for dopant species.

Dopant	Energy [eV]
Al^{3+}	1.71
Mn^{3+}	1.33
Fe^{3+}	2.34
Co^{3+}	1.50
Ga^{3+}	1.51
Sc^{3+}	1.24
Fe^{2+}	4.07
Ni^{2+}	4.51

with smaller dopants preferring an adjacent (nearest neighbor, NN) site to the vacancy, whereas larger dopant cations favor the second coordination shell (next-nearest neighbor, NNN). In a similar approach, we have considered the energetics of simple defect configurations in our perovskite lattice involving pair clusters (M-$V_o^{\bullet\bullet}$) at NN or NNN sites (Fig. 1a), and trimers with one dopant adjacent to the vacancy (NN site) and the other at NN and NNN sites. (Fig. 1b). The cluster binding energies, which are reported in Table 3a and b for pair and trimer configurations, respectively, were calculated according to:

$$E_{\text{bind}} = E_{\text{cluster}} - \sum E_{\text{isolated defect}} \quad (1)$$

In addition to the series of trivalent dopants, Table 3 also lists the corresponding cluster binding energies for Fe^{4+}, which is determined by Mössbauer spectroscopy to be present in significant amounts in even mildly reduced $CaTi(Fe)O_{3-\delta}$.[5,20]

Inspection of Table 3 reveals that simple pair defects and trimers are favorable for the series of trivalent cations, with the exception of Ga^{3+}. There is a general preference for the NN site in both pair and trimer clusters, apart from the cations with the strongest (Ti^{3+}) and weakest binding energies (Sc^{3+} and Ga^{3+}). The weak binding energies observed for Sc^{3+} are reflected in the high oxide-ion conductivity of Sc-substituted $CaTiO_3$,[36] the highest observed in the $CaTiO_3$ system and comparable to that of yttria-stabilized zirconia. The calculated binding energies for Ga^{3+} are also low, but the reported values for oxide-ion conductivity in Ga-doped $CaTiO_3$ are similar to those of the Al-doped phase;[36] this suggests that further optimization of the ion-transport properties of the Ga-containing material is possible. The binding energies observed for the Ti^{3+} cation may, in contrast, result in higher activation energies for oxide-ion transport in reduced $CaTiO_3$. The unfavorable binding energies calculated for the Fe^{4+} cation are expected to enhance the ionic conductivity, in agreement with experimental data.[21] This will be further discussed in Section 2.4.

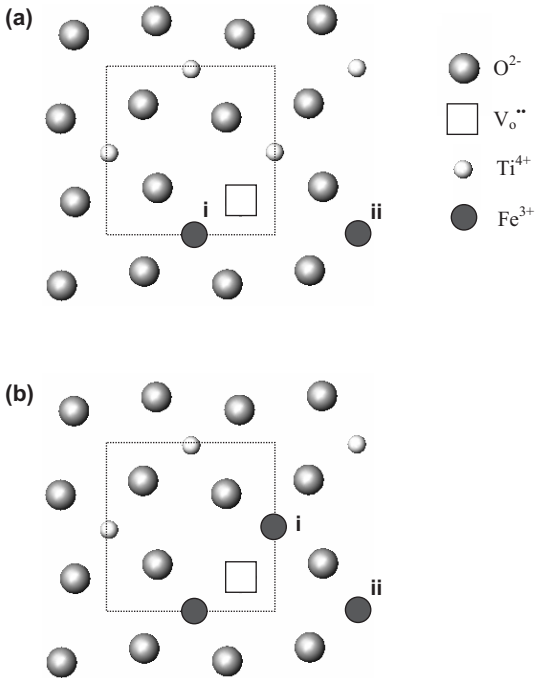

Figure 1. Fe dopant-vacancy cluster configurations in $CaTiO_3$. a) Simple pair defect cluster ($Fe_{Ti}' - V_o^{\bullet\bullet}$) with Fe^{3+} located as nearest neighbor (i) or next-nearest neighbour (ii). b) Trimer defect cluster ($Fe_{Ti}' - V_o^{\bullet\bullet} - Fe_{Ti}'$) with second Fe^{3+} as nearest neighbour (i) or next-nearest neighbour (ii).

Table 3. Binding energies for dopant-vacancy clusters in $CaTiO_3$.
(a) pair clusters

Dopant Species	Defects	Binding energy [eV/defect]	
		NN pair [a]	V + NNN [a]
Al^{3+}	$V_{O2}^{\bullet\bullet}$, Al_{Ti}'	–0.33	+0.06
Ti^{3+}	$V_{O2}^{\bullet\bullet}$, Ti_{Ti}'	–0.40	–0.46
Mn^{3+}	$V_{O2}^{\bullet\bullet}$, Mn_{Ti}'	–0.10	–0.06
Fe^{3+}	$V_{O2}^{\bullet\bullet}$, Fe_{Ti}'	–0.12	–0.08
Co^{3+}	$V_{O2}^{\bullet\bullet}$, Co_{Ti}'	–0.20	–0.04
Ga^{3+}	$V_{O2}^{\bullet\bullet}$, Ga'	+0.05	–0.05
Sc^{3+}	$V_{O2}^{\bullet\bullet}$, Sc_{Ti}'	–0.02	–0.10
Fe^{4+}	$V_{O2}^{\bullet\bullet}$, $Fe_{Ti}^{\times}$	+0.36	+0.00

(b) trimer clusters

Dopant Species	Defects	Binding energy [eV/defect]	
		NN trimer [b]	pair + NNN [b]
Al^{3+}	$V_{O2}^{\bullet\bullet}$, Al_{Ti}'	–0.45	–0.20
Ti^{3+}	$V_{O2}^{\bullet\bullet}$, Ti_{Ti}'	–0.52	–0.44
Mn^{3+}	$V_{O2}^{\bullet\bullet}$, Mn_{Ti}'	–0.12	–0.07
Fe^{3+}	$V_{O2}^{\bullet\bullet}$, Fe_{Ti}'	–0.15	–0.08
Co^{3+}	$V_{O2}^{\bullet\bullet}$, Co_{Ti}'	–0.26	–0.13
Ga^{3+}	$V_{O2}^{\bullet\bullet}$, Ga_{Ti}'	0.08	0.03
Sc^{3+}	$V_{O2}^{\bullet\bullet}$, Sc_{Ti}'	–0.01	–
Fe^{4+}	$V_{O2}^{\bullet\bullet}$, $Fe_{Ti}^{\times}$	+0.49	+0.25

[a] See Figure 1a. [b] See Figure 1b.

2.3. Defect Clusters

2.3.1. Configuration of Complex Defect Clusters

As mentioned earlier, the formation of large dopant-vacancy clusters in doped $CaTiO_3$ has been observed experimentally in the case of $CaTi(Fe)O_{3-\delta}$, and the crystallization of fully ordered phases (e.g., $Ca_2Fe_2O_5$, $Ca_3TiFe_2O_8$) occurs at high Fe contents. These clusters form as mutually perpendicular domains of linear defects, which increase in size with increasing Fe content and annealing time.[18] We note, however, that the microstructure of the undoped phase is similarly characterized by twinned microdomains,[37] which is an additional consideration in the interpretation of the microstructure. Previous simulation work employing a Monte Carlo methodology indicates that oxygen vacancies are preferentially located in the domain walls in the undoped phase.[38] Although the domains in Fe-substituted $CaTiO_3$ may also result, in part, from twinning phenomena, the formation of large dopant-vacancy clusters has a much greater impact on domain evolution, eventually leading to the formation of fully ordered phases for high Fe contents.

The important influence of the microstructure on transport properties has recently been illustrated in $CaTi(Fe)O_{3-\delta}$ ceramics with core/shell microstructures, which show enhanced oxide-ion conductivity at the Fe-rich domain walls.[5] Further understanding of the formation of defect clusters in the doped phase and the microstructure at the atomic level may, therefore, be helpful in unraveling the complex structure–property relationships of the $CaTiO_3$ system.

We first considered the formation of clusters consisting of two oxygen vacancies and four Fe^{3+} cations, limiting possible defect configurations to the *ac* plane containing O2 sites in accordance with the observed ordered structure.[17] Figure 2 provides schematic diagrams of a number of possible defect configurations for the six defects. Three such arrangements are illustrated in Figure 2a, in which adjacent oxygen vacancies are aligned in the [001] direction of the orthorhombic cell (equivalent to the [101] of the parent cubic cell) with three NN Fe^{3+} cations. The fourth Fe^{3+} ion was placed in either position A, B, or C. Two more configurations consisted of 3 Fe^{3+} and 2 $V_o^{\bullet\bullet}$ defects aligned in the [101] direction (Fig. 2b) of the orthorhombic cell, and the fourth Fe^{3+} either in line with the other defects (position D) or isolated from the other defects (position E). The sixth cluster configuration was for two isolated defect trimers (Fig. 2c). Table 4 lists the binding energies for each of these configurations along with the corresponding Fe coordination states. The lowest-energy configuration is observed for the arrangement with Fe^{3+} in position A, with only a slightly higher energy observed when the fourth Fe^{3+} cation is in position B. In both cases the oxygen vacancies lie parallel to [001] such that one of the Fe^{3+} cations is in a tetrahedral coordination environment. The least favorable configurations are those with the vacancy defects aligned in the [101] direction (Fig. 2b), in which there is a 4-fold Fe^{3+} in a square-planar coordination environment.

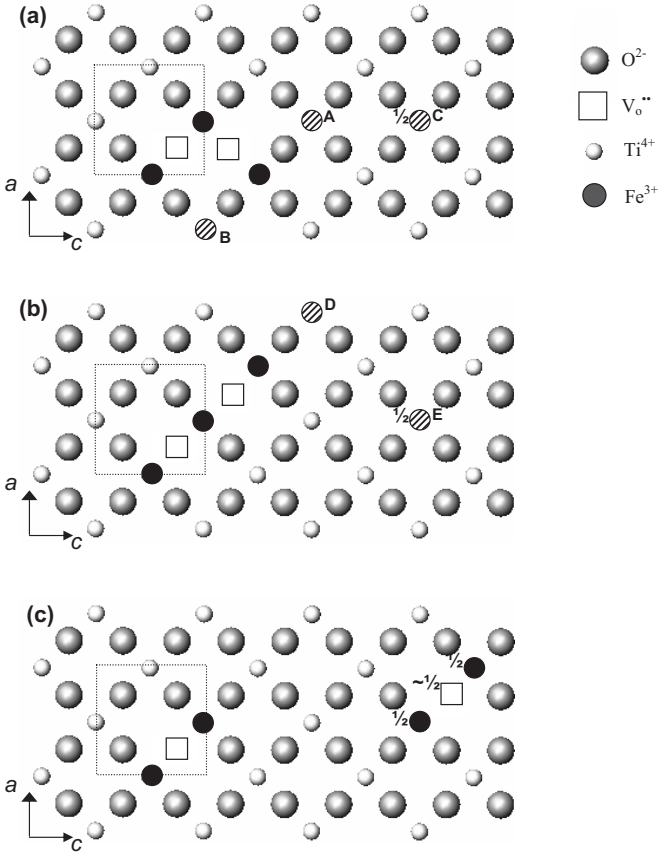

Figure 2. Configurations for complex defect clusters of four Fe^{3+} and two O^{2-} vacancies positioned with respect to the orthorhombic unit cell (outlined, orthorhombic distortion not represented for clarity). Alternative configurations for Fe^{3+} cations within a cluster are shown as hatched spheres.

Table 4. Binding energies of clusters with two oxygen vacancies and four Fe^{3+} cations in the *ac* plane of $CaTiO_3$.

Configuration [a]	Fe coordination			Binding energy per defect [eV]
	4-fold	5-fold	6-fold	
A	1	2	1	–0.23
B	1	2	1	–0.20
C	1	2	1	–0.14
D	1	2	1	–0.01
E	1	2	1	0.06
F	0	4	0	–0.13

[a] See Figure 2.

These results are consistent with the formation of chains of oxygen vacancies aligned along the [001] direction ($[101]_{cubic}$), resulting in brownmillerite-like defects. McCammon et al.[19] have proposed a model for the short-range ordering of vacancies within the clusters in accordance with Fe coordination states determined from Mössbauer data. A high proportion of Fe^{3+} is observed to reside in a hexacoordinated environment and an equivalent proportion of pentacoordinated Ti^{4+} must therefore be present at vacancy-chain terminations; the relative proportion of pentacoordinated Ti^{4+} will depend on the average length of the vacancy chains, which is in turn dependent on the Fe content and the temperature. To test this hypothesis, we calculated the energy of the most favorable defect configuration with one Ti^{4+} cation placed on a pentacoordinated site and one Fe^{3+} cation on a hexacoordinated site, isolated from the defect cluster. The energy of this latter configuration was –0.22 eV/defect, which is essentially equivalent to that of configuration A (–0.23 eV/defect). We may expect, therefore, a high proportion of Ti^{4+} in pentacoordinated sites, in accordance with the proposed model of short-range clustering.

2.3.2. Location of Fe^{4+} Species

As mentioned previously, the presence of Fe^{4+} appears to have an important influence on the ionic conductivity in nonreducing atmospheres and may be closely associated with the formation of defect aggregates. In order to determine the preferred location for Fe^{4+} within a cluster, a series of cluster calculations were carried out, again adopting the most favored

configuration A, placing Fe^{4+} in each of the four positions i–iv shown in Figure 3. A fifth configuration was also considered, with Fe^{4+} isolated from the cluster in position v, and with position iv in the cluster occupied by Ti^{4+} rather than Fe^{3+} in order to maintain a consistent cation ratio. The results listed in Table 5 indicate that the preferred location for the Fe^{4+} species is a hexacoordinated site rather than a pentacoordinated site with the vacancy in the first coordination shell (i.e., an NN pair cluster); this agrees with the simple defect-cluster calculations (Table 3), which also indicate that an arrangement with adjacent $V_o^{\bullet\bullet}$ and Fe^{4+} species is energetically unfavorable. The result is in accord with recent reports that suggest that Fe^{4+} tends to occupy sites at the domain boundaries, promoting the termination of chains of defects and increasing disorder.[5,39]

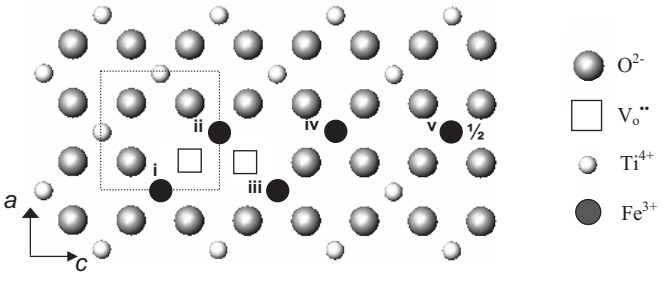

Figure 3. Possible locations for an Fe^{4+} cation in a favorable complex cluster arrangement of four Fe and two O vacancies (orthorhombic distortion not represented for clarity). The cluster consists of either three Fe^{3+} and two O vacancies with the fourth position (i, ii, ii, iv) occupied by Fe^{4+} and the isolated position (v) occupied by Ti^{4+}; or of three Fe^{3+} positions (i, ii, iii) and two O vacancies with (v) occupied by $Fe^{4+}$and (iv) occupied by Ti^{4+}.

Table 5. Binding energies for different Fe^{4+} positions in the cluster.

Fe^{4+} position [a]	Fe^{4+} coordination	Binding energy per defect [eV]
i	5-fold	0.00
ii	4-fold	0.18
iii	5-fold	–0.01
iv	6-fold	–0.15
v	6-fold	–0.14

[a] See Figure 3.

2.3.3. Mutually Perpendicular Clusters

The formation of mutually perpendicular domains is commonly observed in $CaTi(Fe)O_{3-\delta}$, but the manner in which the linear defects may intersect and the proposed importance of domain walls with regards to the ionic transport is not fully understood. We have carried out a series of calculations of two short linear clusters (each consisting of two $V_o^{\bullet\bullet}$ and four Fe_{Ti}') placed perpendicular to one another, parallel to ***c*** and ***a,*** but at various distances from each other. The two most favorable arrangements are shown in Figure 4 with energies of ca. –0.3 eV/defect for each. In both configurations there are two tetra-, four penta- and two hexacoordinated cation sites. In accordance with the preference of Fe^{4+} for 6-fold coordination

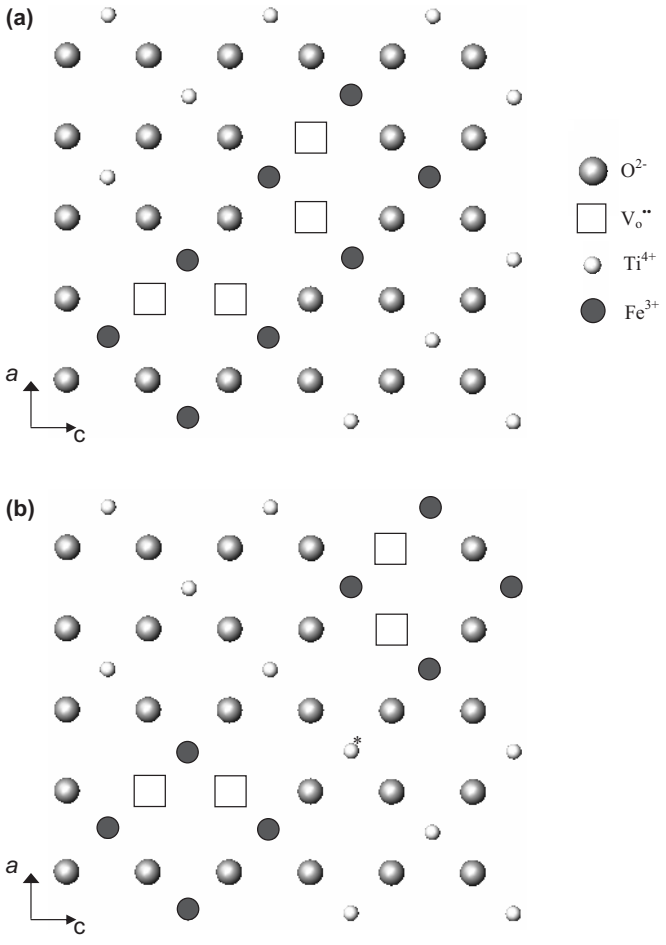

Figure 4. Favorable arrangements for two complex defect clusters, each consisting of four Fe^{3+} and two O vacancies, oriented perpendicular to one another. The asterisk marks the most likely position for Fe^{4+} in the configuration with the two clusters further apart.

and the observed influence of Fe^{4+} on shortening defect clusters, it is likely that the presence of Fe^{4+} results in the defect configuration illustrated in Figure 4b; the most probable location for Fe^{4+} is marked with an asterisk.

2.4. Oxide-Ion Migration

Optimization of oxide-ion conductivity is one of the principal objectives in the investigation of mixed conductors for ceramic-membrane reactors. A number of studies have illustrated the value of atomistic simulations in probing the energetics of oxygen migration to gain an understanding of the mechanistic features of oxygen transport in polar solids.[32,40–42]

We have focused on oxide-ion migration within the orthorhombic polymorph of calcium titanate, which is adopted over a wide range of temperatures relevant to the operation of a ceramic membrane reactor (< 800 °C). In this symmetry, the eight equivalent pathways found in the cubic perovskite between nearest-neighbor oxygens degenerate such that an oxygen on an O2 site (Fig. 5) may migrate to another O2 site, approximately parallel to the ***a*** or ***c*** directions (indicated by black and

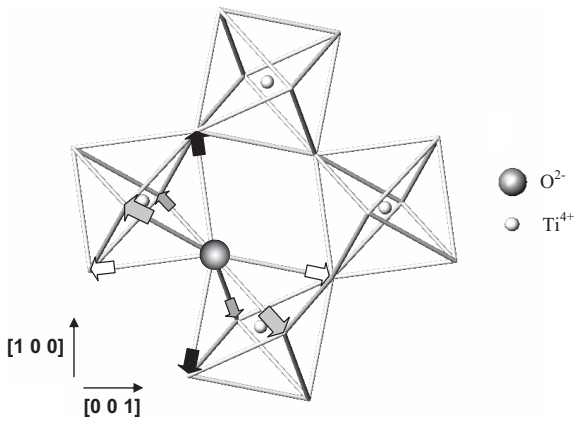

Figure 5. The orthorhombic $CaTiO_3$ structure represented as corner-sharing TiO_6 octahedra. Arrows indicate oxide-ion migration pathways: O2–O2 hops in the *ac* plane result in migration parallel to the [100] and [001] directions, indicated by black and white arrows, respectively; O2–O1 hops, represented by gray arrows, result in migration parallel to [010].

white arrows in Fig. 5, respectively), or to one of four O1 sites at nonequivalent distances (indicated by grey arrows). Two of the O1–O2 distances are slightly shorter (ca. 2.75 Å) than the other two (ca. 2.83 Å); these shorter O1-O2 distances form a continuous zigzagging pathway parallel to ***b***.

The energy profiles for direct linear migration in each of the three directions were calculated by placing the oxide ion at intermediate positions between adjacent oxygen vacancies along the edges of a TiO_6 octahedron (Fig. 5). The effective charge of a migrating oxide ion differs only slightly from that in a lattice site, as found by quantum-mechanical methods for an "interstitial" oxygen in $KNbO_3$.[43] This validates the adoption of the lattice oxygen potentials for the migrating anion. The energy for linear migration, listed in Table 6, is lower along **b** ($E_a = 0.57$ eV) than along **a** or **c** ($E_a = 0.62$ and 0.73 eV, respectively). Correspondingly, we note that the shortest and longest hopping distances are along the ***b*** and ***c*** directions, respectively, despite the fact that ***c*** is the shortest "pseudo-cubic" cell-edge parameter, because of the octahedral tilting in orthorhombic $CaTiO_3$.

Previous simulations of perovskite oxides found that the migrating oxide ion does not follow a direct linear pathway along the octahedral edge but instead curves away slightly from the central cation.[24,41,42] Recently, experimental work has confirmed a curved oxide-ion migration pathway in a $LaGaO_3$-based electrolyte.[44] The minimum in the energy surface between two oxygen sites was located in a manner similar to a previous study[42] and found to be at ca. 0.17 Å from the midpoint of the octahedral edge for migration along ***a***, and slightly further, ca. 0.21 Å, in the ***b*** and ***c*** directions. Again, the lowest energy pathway is along ***b*** with an activation energy of 0.43 eV (Table 6); values of 0.51 and 0.55 eV are found for migration along ***a*** and ***c***, respectively. The migration profiles were slightly asymmetric, most likely because of the variation in distance to neighboring Ca cations along the migration pathway in the distorted, orthorhombic structure.

Our results are in good agreement with the literature value of 0.56 eV for oxide-ion migration obtained from the temperature dependence of the oxygen chemical diffusion coefficient of $CaTiO_3$ single crystals.[27] Data were collected in a reducing H_2/H_2O atmosphere, corresponding to $pO_2 \approx 10^{-10}$ Pa in the range 1100–1300 °C. Higher values were obtained with the same technique for ceramic samples: 0.68 eV in air and 1.39 eV at $pO_2 \approx 10$ Pa,[45] which may indicate that impurities or grain boundaries lead to higher resistances in the polycrystalline materials.

The energy profiles for curved migration in the slightly preferred ***b*** direction for octahedra with central Fe^{3+} and Fe^{4+} cations were also calculated and are shown in Figure 6, along with the corresponding profile for the octahedron centered on Ti^{4+}. The minimum energy in the curved pathway was found to be only a little further from the Fe^{3+} cation, as one may expect when considering the ionic radii (0.605 Å, 0.585 Å, and 0.645 Å for Ti^{4+}, Fe^{4+} and Fe^{3+}, respectively).[46] However, oxygen migration is much less favorable between sites adjacent to an Fe^{3+} cation compared with migration adjacent to Ti^{4+}, indicating the importance of electrostatic effects. This accords with the favorable binding energies of $Fe_{Ti}' - V_o^{\bullet\bullet}$ clusters (Table 3) and higher activation energies for oxide-ion transport observed for Fe-doped calcium titanate relative to the undoped phase. A value for ionic conduction as high as 2.9 eV has been reported for $CaTi_{0.8}Fe_{0.2}O_{3-\delta}$ in reducing conditions, where all the Fe is expected to be in the +3 valence state.[47] However, the energy for vacancy migration along a curved pathway adjacent to the Fe^{4+} species is only slightly higher than the corresponding value

Table 6. Calculated energies for oxygen-vacancy migration.

Migration direction [a]	Mean hopping distance [Å]	E_a [eV]	
		Linear	Curved
a	2.76	0.62	0.51
b	2.75	0.57	0.43
c	2.81	0.73	0.55

[a] See Figure 5.

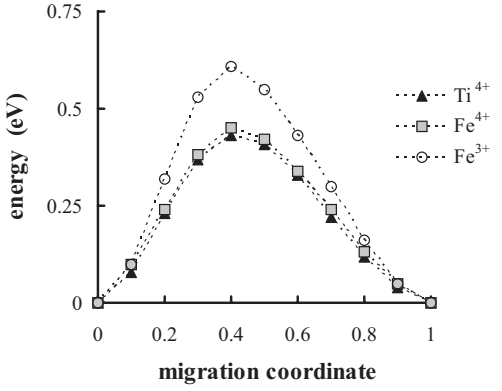

Figure 6. Energy profiles of oxygen-vacancy migration along a curved pathway adjacent to the edge of an octahedron centered on Fe^{3+}, Fe^{4+}, and Ti^{4+} cations.

adjacent to Ti^{4+}. This indicates that ionic transport in materials with a high Fe^{4+}/Fe(total) ratio may be enhanced through lowering of the activation energy, in addition to the enhanced disorder we may expect because of the preference of Fe^{4+} for hexacoordinated sites. The simulations are consistent with the much lower activation enthalpies for oxide-ion transport measured for the Fe-substituted materials under oxidizing conditions, namely 0.78 and 0.94 eV,[5,21] than for reducing atmospheres. This large difference in activation energy between completely-reduced and Fe^{4+}-containing materials provides support for the argument that the domain walls provide a favored pathway for ionic transport,[5] as also proposed for pure calcium titanate[38] and other related perovskites.[48]

3. Conclusions

New atomic-scale insight into doped $CaTiO_3$ materials has been derived by advanced simulation techniques relevant to their electrochemical applications, particularly as a mixed-conducting membrane for oxygen separation and partial oxidation. First, dopant-vacancy association is predicted to be favorable for simple pair clusters ($M_{Ti}' - V_o^{\bullet\bullet}$) and neutral trimers ($M_{Ti}' - V_o^{\bullet\bullet} - M_{Ti}'$), where M is, for example, Sc, Mn or Fe. The large binding energies found for the Ti^{3+} electronic species should result in higher activation energies for ionic conduction in the reduced material. Second, the binding energies of larger clusters ($4\,M_{Ti}' - 2\,V_o^{\bullet\bullet}$) were calculated, and the lowest-energy configurations found for oxygen vacancies aligned in the $[101]_{cubic}$ direction in accordance with the development of short-range or nanoscale clusters of brownmillerite-like domains. Third, the role of Fe^{4+} in domain formation in the Fe-doped material was analyzed, and the preferred location for Fe^{4+} was found to be a hexacoordinated site. This supports the hypothesis that Fe^{4+} promotes the termination of defect chains and increases disorder. Finally, oxide-ion migration in the orthorhombic unit cell of $CaTiO_3$ is calculated to occur preferentially in the [010] direction (space group, *Pnma*) with a lower activation energy calculated for a curved rather than linear trajectory. The results are consistent with the observation that $CaTi(Fe)O_{3-\delta}$ under oxidizing conditions, with a higher proportion of Fe^{4+}, has lower activation energies for oxide-ion transport than under reducing conditions.

4. Experimental

Comprehensive reviews of the atomistic simulation techniques employed in the General Utility Lattice Program (GULP) code [49] have been given elsewhere [40]. A short synopsis is provided as Supplementary Information. The potentials describing interatomic interactions are represented by ionic pairwise potentials, which include the long-range Coulomb term and an analytical function to model overlap repulsions and van der Waals forces. The potential parameters A_{ij}, ρ_{ij}, and C_{ij} describing the short-range ion–ion interactions were taken directly from previous simulations of perovskites for the Ti^{4+}–O^{2-}, Fe^{3+}–O^{2-}, and O^{2-}–O^{2-} interactions (Table 7) [30,32,50]; minor refinement of the A and ρ parameters for the Ca–O interaction was carried out by fitting to the experimental orthorhombic crystal structure. The potential parameters for Fe^{4+} (Table 7) were determined by fitting to the experimental structure of perovskite $SrFeO_3$ [51].

Calcium titanate exhibits a sequence of structural phase transitions on heating, shared by many perovskite systems: orthorhombic (*Pnma*) → tetragonal (*I4/mcm*) → cubic ($Pm\bar{3}m$) [52]. Becerro and coworkers [18,53,54] have studied phase fields in Fe-doped compositions and reported that the temperature of these phase boundaries decreases with Fe content. For a membrane of $CaTi_{0.8}Fe_{0.2}O_{3-\delta}$ with a working temperature of ca. 800 °C, orthorhombic symmetry is observed, but with considerable short-range clustering of the defect species.

Table 7. Interatomic potentials for $CaTiO_3$ and $CaTi(Fe)O_{3-\delta}$.

(i) Buckingham potentials (cut-off = 15 Å)

Interaction	A [eV]	ρ [eV]	C [eV Å^{-6}]
$Ca^{2+}\cdots O^{2-}$	1340.18	0.3214	0.00
$Ti^{4+}\cdots O^{2-}$ [a]	877.2	0.38096	9.00
$Fe^{3+}\cdots O^{2-}$ [b]	1156.36	0.3299	0.00
$Fe^{4+}\cdots O^{2-}$	1540.0	0.3299	0.00
$O^{2-}\cdots O^{2-}$ [c]	22764.0	0.1490	43.00

(ii) Shell model [d]

Species	Y [e]	k [eV Å^{-2}]
Ca^{2+} [e]	3.135	110.2
Ti^{4+} [a]	–35.863	65974.0
Fe^{3+} [b]	4.97	304.7
Fe^{4+}	5.97	304.7
O^{2-} [c]	–2.389	18.41

[a] See Akhtar et al. [30] and Lewis et al. [50]. [b] See Cherry et al. [32]. [c] See Alkhtar et al. [30], Cherry et al. [32], and Lewis et al. [50]. [d] Y and k refer to the shell charge and harmonic force constant, respectively. [e] See Lewis and Catlow [33].

Before performing defect calculations, the orthorhombic crystal structure of $CaTiO_3$ was optimized (minimized with respect to energy) under constant-pressure conditions. On relaxation of the unit-cell parameters and atomic positions, the potentials successfully reproduced the observed structure, as indicated by good agreement with the experimental unit-cell parameters [55] (error < 1 %) and bond lengths (Table 8a).

Defect calculations were also carried out for the doped phase $CaTi_{0.8}Fe_{0.2}O_{3-\delta}$, which exhibits good mixed conductivity. For this, a supercell ($1 \times 1 \times 5$ orthorhombic unit cells) of $CaTi_{0.8}Fe_{0.2}O_{3-\delta}$ [54] was constructed, in space group *P1*, to avoid partial occupancies. The supercell had an atomic content of $Ca_{20}Ti_{16}Fe_4O_{58}$, with the four Fe atoms and two O vacancies placed in the lowest-energy configuration described in Section 2.3. The structure was also optimized under constant pressure conditions, again resulting in good agreement with the experimental unit-cell parameters of the equivalent single orthorhombic cell (Table 8b) [54].

Received: July 18, 2006
Revised: September 25, 2006
Published online: February 9, 2007

[1] X. S. Wang, C. N. Xu, H. Yamada, K. Nishikubo, X. G. Zheng, *Adv. Mater.* **2005**, *17*, 1254.
[2] H. N. Lee, H. M. Christen, M. F. Chisholm, C. M. Rouleau, D. H. Lowndes, *Nature* **2005**, *433*, 395.
[3] Z. X. Chen, Y. Chen, Y. S. Jiang, *J. Phys. Chem. B* **2002**, *106*, 9986.
[4] H. Iwahara, T. Esaka, T. Mangahara, *J. Appl. Electrochem.* **1988**, *18*, 173.
[5] F. M. Figueiredo, V. V. Kharton, J. C. Waerenborgh, A. P. Viskup, E. N. Naumovich, J. R. Frade, *J. Am. Ceram. Soc.* **2004**, *87*, 2252.

Table 8. Calculated and experimental properties of $CaTiO_3$ and $CaTi_{0.8}Fe_{0.2}O_{3-\delta}$

(a) $CaTiO_3$

Lattice energy: –150.88 eV per formula unit

Unit-cell parameters [Å]			
Experimental [a]		Calculated	Difference [%]
a	5.4423	5.4446	0.04
b	7.6401	7.6802	0.52
c	5.3796	5.3907	0.21

Bond lengths [Å]			
Bond	Experimental [a]	Calculated	Difference [%]
Ti-O1 × 2	1.950	1.977	1.36
Ti-O2 × 2	1.955	1.967	0.61
Ti-O2 × 2	1.959	1.972	0.33
Ca-O1 × 1	2.359	2.288	–3.10
Ca-O1 × 1	2.473	2.499	1.04
Ca-O1 × 1	3.035	3.026	0.30
Ca-O1 × 1	3.051	3.129	2.49
Ca-O2 × 2	2.379	2.304	–3.25
Ca-O2 × 2	2.617	2.660	1.62
Ca-O2 × 2	2.663	2.726	2.31
Ca-O2 × 2	3.236	3.241	0.15

(b) $CaTi_{0.8}Fe_{0.2}O_{3-\delta}$

Lattice energy: –143.04 eV per formula unit

Unit-cell parameters (1 × 1 × 5) supercell			
Experimental [b]		Calculated	Difference [%]
a/Å	5.4359	5.4573	0.39
b/Å	7.6623	7.6117	–0.60
5 × c/Å	27.0185	27.0709	0.14
α	90.0°	89.96°	–0.04
β	90.0°	90.02°	0.02
γ	90.0°	90.06°	0.07

[a] See Sasaki et al. [55]. [b] See Becerro et al. [54].

[6] E. Chinarro, J. R. Jurado, F. M. Figueiredo, J. R. Frade, *Solid State Ionics* **2003**, *160*, 161.
[7] V. V. Lemanov, A. V. Sotnikov, E. P. Smirnova, M. Weinacht, R. Kunze, *Solid State Commun.* **1999**, *110*, 611.
[8] J. Hao, W. Si, X. X. Xi, R. Guo, A. S. Bhalla, L. E. Cross, *Appl. Phys. Lett.* **2000**, *76*, 3100.
[9] V. V. Lemanov, A. V. Sotnikov, E. P. Smirnova, M. Weihnacht, *Appl. Phys. Lett.* **2002**, *81*, 886.
[10] K. L. Smith, N. J. Zaluzec, *J. Nucl. Mater.* **2005**, *336*, 261.
[11] M. Manso, M. Langlet, J. M. Martinez-Duart, *Mater. Sci. Eng. C* **2003**, *23*, 447.
[12] a) A. Thursfield, I. S. Metcalfe, *J. Mater. Chem.* **2004**, *14*, 2475. b) H. J. M. Bouwmeester, A. J. Burgraaf, in *Fundamentals of Inorganic Membrane Science and Technology* (Eds: A. J. Burgraaf, L. Cot), Elsevier, Amsterdam **1996**, pp. 435–528.
[13] H. Itoh, H. Asano, K. Fukuroi, M. Nagata, H. Iwahara, *J. Am. Ceram. Soc.* **1997**, *80*, 1359.
[14] V. V. Kharton, F. M. Figueiredo, A. V. Kovalevsky, A. P. Viskup, E. N. Naumovich, J. R. Jurado, J. R. Frade, *Defect Diffus. Forum* **2000**, *186–187*, 119.
[15] Y. Teraoka, H. M. Y. Zhang, K. Okamoto, N. Yamazoe, *Mater. Res. Bull.* **1988**, *23*, 51.
[16] J. W. Stevenson, T. R. Armstrong, R. D. Carneim, L. R. Pederson, W. J. Weber, *J. Electrochem. Soc.* **1996**, *143*, 2722.
[17] J.-C. Grenier, G. Schiffmacher, P. Caro, M. Pouchard, P. Hagenmuller, *J. Solid State Chem.* **1977**, *20*, 365.
[18] A. I. Becerro, F. Langenhorst, R. Angel, S. Marion, C. McCammon, F. Seifert, *Phys. Chem. Chem. Phys.* **2000**, *2*, 3933.
[19] C. McCammon, A. I. Becerro, F. Langenhorst, R. Angel, S. Marion, F. Seifert, *J. Phys. Condens. Matter* **2000**, *12*, 2969.
[20] J. C. Waerenborgh, F. M. Figueiredo, J. R. Jurado, J. R. Frade, *J. Phys. Condens. Matter* **2001**, *13*, 8171.
[21] F. M. Figueiredo, J. C. Waerenborgh, V. V. Kharton, H. Näfe, J. R. Frade, *Solid State Ionics* **2003**, *156*, 371.
[22] M. S. Islam, R. A. Davies, *J. Mater. Chem.* **2004**, *14*, 86.
[23] E. N. Naumovich, M. V. Patrakeev, V. V. Kharton, M. S. Islam, A. A. Yaremchenko, J. R. Frade, F. M. B. Marques, *Solid State Ionics* **2006**, *177*, 457.
[24] R. Glöckner, M. S. Islam, T. Norby, *Solid State Ionics* **1999**, *122*, 145.
[25] J. Wu, R. A. Davies, M. S. Islam, S. M. Haile, *Chem. Mater.* **2005**, *17*, 846.
[26] C. M. Freeman, C. R. A. Catlow, *J. Solid State Chem.* **1990**, *85*, 65.
[27] W. L. George, R. E. Grace, *J. Phys. Chem. Solids* **1969**, *30*, 889.
[28] U. Balachandran, B. Odekirk, N. G. Eror, *J. Solid State Chem.* **1982**, *41*, 185.
[29] K. Ueda, H. Yanagi, H. Hosono, H. Kawazoe, *Phys. Rev. B: Condens. Matter Mater. Phys.* **1997**, *56*, 12 998.
[30] M. J. Akhtar, Z. Akhtar, R. A. Jackson, C. R. A. Catlow, *J. Am. Ceram. Soc.* **1995**, *78*, 421.
[31] R. A. Davies, M. S. Islam, J. D. Gale, *Solid State Ionics* **1999**, *126*, 323.
[32] M. Cherry, M. S. Islam, C. R. A. Catlow, *J. Solid State Chem.* **1995**, *118*, 125.
[33] G. V. Lewis, C. R. A. Catlow, *J. Phys. C* **1985**, *18*, 1149.
[34] H. D. B. Jenkins, H. K. Roobottom, in *CRC Handbook of Chemistry and Physics*, 84th ed. (Ed: D. R. Lide), CRC Press, Boca Raton, FL **2003**, pp. 12–28.
[35] M. S. Khan, M. S. Islam, D. R. Bates, *J. Mater. Chem.* **1998**, *8*, 2299.
[36] S. Hashimoto, H. Kishimoto, H. Iwahara, *Solid State Ionics* **2001**, *139*, 179.
[37] Y. Jiang, R. Guo, A. S. Bhalla, *J. Electroceram.* **1998**, *2*, 199.
[38] M. Calleja, M. T. Dove, E. K. H. Salje, *J. Phys. Condens. Matter* **2003**, *15*, 2301.
[39] J. Canales-Vázquez, F. M. Figueiredo, J. C. Waerenborgh, W. Zhou, J. R. Frade, J. T. S. Irvine, *J. Solid State Chem.* **2004**, *177*, 3105.
[40] C. R. A. Catlow, in *Solid State Chemistry: Techniques* (Eds: A. K. Cheetham, P. Day), Clarendon, Oxford **1987**, pp. 231–277.
[41] M. S. Islam, *Solid State Ionics* **2002**, *154–155*, 75.
[42] G. C. Mather, M. S. Islam, *Chem. Mater.* **2005**, *17*, 1736.
[43] P. W. M. Jacobs, E. A. Kotomin, R. I. Eglitis, *J. Phys. Condens. Matter* **2000**, *12*, 569.
[44] a) M. Yashima, K. Nomura, H. Kageyama, Y. Miyazaki, N. Chitose, K. Adachi, *Chem. Phys. Lett.* **2003**, *380*, 391. b) M. M. Gunter, C. Korte, G. Brunauer, H. Boyson, M. Lerch, E. Suard, *Z. Anorg. Allg. Chem.* **2005**, *631*, 1277.
[45] T. Bak, J. Nowotny, C. C. Sorrel, *J. Phys. Chem. Solids* **2004**, *65*, 1229.
[46] R. D. Shannon, *Acta Crystallogr. A* **1976**, *32*, 751.
[47] S. Marion, A. I. Becerro, T. Norby, *Ionics* **1999**, *5*, 385.
[48] M. Calleja, E. K. H. Salje, S. A. Hayward, W. T. Lee, *Acta Crystallogr. A* **2005**, *61*, 3.
[49] J. D. Gale, *J. Chem. Soc., Faraday Trans.* **1997**, *93*, 629.
[50] G. V. Lewis, C. R. A. Catlow, *J. Phys. Chem. Solids* **1986**, *47*, 89.
[51] J. P. Hodges, S. Short, J. D. Jorgensen, X. Xiong, B. Dabrowski, S. M. Mini, C. W. Kimball, *J. Solid State Chem.* **2000**, *151*, 190.
[52] S. A. T. Redfern, *J. Phys. Condens. Matter* **1996**, *8*, 8267.
[53] A. I. Becerro, C. McCammon, F. Langenhorst, R. J. Angel, F. Seifert, *Phase Transitions* **1999**, *69*, 133.
[54] A. I. Becerro, S. A. T. Redfern, M. A. Carpenter, K. S. Knight, F. Seifert, *J. Solid State Chem.* **2002**, *167*, 459.
[55] S. Sasaki, C. T. Prewitt, J. D. Bass, W. A. Schulze, *Acta Crystallogr. C* **1987**, *43*, 1668.